Tribology International 187 (2023) 108696

Contents lists available at ScienceDirect

Tribology International

journal homepage: www.elsevier.com/locate/triboint

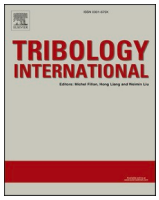

Theoretical and experimental analysis of the centrifugal micro hydrodynamic axial-thrust bearing

Huaiyu Zuo, Song Xue, Tao Hong, Guanying Xing, Jiacheng Han, Jinlong Ma, Run Hu, Xiaobing Luo *

School of Energy and Power Engineering, Huazhong University of Science and Technology, Wuhan 430074, China

ARTICLE INFO

Keywords:
Hydrodynamic axial-thrust bearing
Flow mechanism
Load capacity

ABSTRACT

The novel centrifugal micro hydrodynamic axial-thrust bearing has been demonstrated to substantially mitigate the wear in hydrodynamic suspension micropumps. To further elevate the bearing performance, the flow mechanism is systematically analyzed via numerical simulations and experiments in this work. The effects of various properties of bearing on the performance are explored and explained. Results indicate that the load capacity augments with the growth of inlet-suction flow rate and with the reduction of rotational speed. Meanwhile, it initially decreases and then increases as fluid film thickness expands. Further, the bearing exhibits proper stiffness and adaptable anti-abrasion when thickness maintains 0.3 mm. This study provides a profound understanding of centrifugal micro hydrodynamic axial-Thrust bearing, and identifies its optimization measures.

1. Introduction

Centrifugal micropumps are extensively utilized in the electronics cooling, aerospace, and communication [1–3] domains, with the bearing constituting a key component. Nevertheless, conventional centrifugal micropumps suffer from the inevitable contact wear in the traditional shaft bearing, thus resulting in short life and low reliability of the devices. To mitigate this issue, a hydrodynamic bearing system has been proposed to enhance the anti-attrition property of micropumps [4–6]. This system utilizes a pressurized fluid that forms a radial and axial hydrodynamic thrust bearing between the rotating and stationary components. It enables omnidirectional support of the rotating component while minimizing contact with the stationary component's surface. This contributes to near-zero abrasion in the micropump, significantly improving the device's performance and durability.

To date, numerous studies have been dedicated to the investigation of hydrodynamic axial thrust bearings. Initially, pad thrust bearings garnered significant attention in the realm of industrial research and application. This led to an in-depth analysis of diverse pad thrust bearings for the design and development of high-performance bearings, encompassing the investigation of thrust bearings featuring distinct surface profiles on the pads. Charnes et al. reported a stepped pad thrust bearing with a higher load capacity than conventional plane inclined thrust bearings [7], and Naduvinamani et al. studied a series of converging wedge-shaped slider bearings and observed a significant increase in pressure for exponential and hyperbolic sliders [8]. The number of pads has also been under scrutiny, with Lai et al. comparing the performance characteristics of rotor-bearing systems with different thrust pad partitions [9]. Furthermore, the application of various surface textures on hydrodynamic axial thrust bearings has been widely investigated due to their ability to enhance load-carrying capacity and reduce the coefficient of friction [10]. In 1966, Hamilton et al. reported that micro-textured surfaces could improve load capacity and noted that cavitation occurs in the voids between neighboring asperities, which was responsible for the observed load support [11]. Subsequently, the performance of thrust bearings with variable shapes (such as rectangular, triangular, circular and bionic-shape etc.) and sizes of surface textures were explored [12–18]. The methods for optimization of texture shape were also under discovery [19–21].

While the hydrodynamic thrust bearings discussed above have demonstrated superior performance and have been widely utilized in various industries, their application in high-speed micropumps is limited by several factors. Firstly, the manufacturing of surface textures or various structures required for these bearings is a complex process, leading to increased costs and assembly time. Additionally, the presence of micro dimples and grooves in these bearings significantly raises the likelihood of blockages and corrosion in micropumps. In cases where these characteristics fail to meet the demands of mass production and

* Corresponding author.
E-mail address: Luoxb@hust.edu.cn (X. Luo).

https://doi.org/10.1016/j.triboint.2023.108696
Received 27 April 2023; Received in revised form 2 June 2023; Accepted 10 June 2023
Available online 12 June 2023

stable operation of micropumps, Centrifugal Micro Hydrodynamic Axial-thrust Bearing (CMHAB) was proposed in our previous works [4–6]. This bearing, which eliminates the complex surface textures and structures, features a simplistic structure and cost-effective design while ensuring the smooth operation of the rotor. However, the flow mechanism in micro hydrodynamic axial-thrust bearings is not clear, which hinders its development and optimization.

In this work, the inherent mechanism and optimization method of CMHAB is further explored. In place of simulating the flow field in the entire micropump, a split-off model of CMHAB is developed and subjected to boundary conditions consistent with the working environment within the micropump. From the calculation results of this model, we deduce the flow patterns and characteristics, providing clarifications into the inherent mechanism of CMHAB. Additionally, a measuring rig is proposed. It is built based on the operation process of CMHAB to examine the actual operation and measure the load capacity. Meanwhile, we comprehensively investigate the influence and impacting mechanism of key factors (including inlet-suction flow rate Q, rotational speed n, and fluid film thickness δ) on bearing performance by CFD simulation and experiments, and identify the optimal value of the parameters. The outcomes of this study have significant implications for the design and optimization of micro hydrodynamic axial-thrust bearings and hydrodynamic suspension micropumps.

2. Methods

2.1. Mathematical modeling

2.1.1. Geometry

Fig. 1a illustrates the structure of the micropump with hydrodynamic bearing system. In micropumps, the rotor is a dynamic component that rotates within the sleeve, driven by an external motor, while the sleeve serves as a stationary component to separate the motor stator from the liquid. Fig. 1b displays the fluidic channel within the micropump. During operation, fluid enters through the rotor's central hole driven by the pressure difference between the upper and lower domains of the rotor center. It floods the rotor's bottom to form a fluid film, and then flows out through the gap between the rotor and the sleeve. Consequently, the fluid situated between the rotor bottom and sleeve creates the CMHAB.

To simulate fluid flow and load capacity within the CMHAB, the lower region of the fluidic channel illustrated in Fig. 1b is isolated and utilized as the three-dimensional computational domain of the CMHAB. This domain is modeled based on its geometry and spatial dimensions (Fig. 2a). It encompasses the inlet fluid flow passage (rotor center hole region), fluid film region, and outlet fluid flow passage (region between the rotor sidewall and sleeve sidewall). Dimension parameters for the CMHAB are denoted in Fig. 2a-b. Assuming smooth rotor and sleeve surfaces, the rotor center hole diameter (D_{ri}) is 1.6 *mm*, the rotor outer diameter (D_{ro}) is 12.66 *mm*, the sleeve inner diameter (D_s) is 12.8 *mm*, and the height of the rotor side surface (l) is 6 *mm*. The eccentric distance of rotor is uniformly set to 35 μm according to the actual operation of the micropump and pre-analysis. Three control variables are considered when studying fluid flow and load capacity in CMHAB: inlet-suction flow rate (Q), rotor speed (n), and fluid film thickness at the bottom (δ). Table 1 presents a comprehensive dataset concerning basic bearing geometry, operating parameters, and fluid property values.

2.1.2. Mesh

The computational domain is partitioned using the Gambit structured mesh method, with Fig. 2c displaying the mesh representation of the fluid fields. To enhance the accuracy of numerical results, conventional grids are generated within the fluid domain, and the grids near the wall are processed to accurately calculate fluid flow within the boundary layer. In this study, the grid height of the first layer near the wall is determined using a specific formula to maintain the wall y + value within a reasonable range. Table 2 presents their specific values at various positions.

$$\Delta y = \frac{y^+ \mu}{\rho u_\tau} = \frac{y^+ x}{\mathrm{Re}\sqrt{\frac{C_f}{2}}} = \frac{y^+ v}{u\sqrt{\frac{0.014}{\mathrm{Re}_x^{\frac{1}{7}}}}} = 8.6 \bullet y^+ \frac{v}{u} \mathrm{Re}_x^{\frac{1}{14}} \tag{1}$$

A grid independence study has been conducted to determine the appropriate number of cells for accurate numerical results. For the fluid field with a fluid film thickness (δ) of 1 *mm*, five distinct element sizes are selected for this investigation. Table 3 displays the mesh specifications for the overall computational domain and the axial load capacity on the rotor. As shown in the table, the coarser mesh yields a higher axial load capacity compared with the finer mesh. However, the results corresponding to different mesh densities exhibit minimal variation. Taking both calculation cost and accuracy into account, a mesh scheme with approximately 3.635 million cells is chosen for the fluid field with a fluid film thickness of 1 *mm*. A similar approach is employed to determine the number of mesh cells for fluid fields with alternative fluid film thicknesses.

2.1.3. Governing equation and assumptions

In the present study, the flow is considered to be isothermal, and the minimum pressure of CMHAB far exceeds the vapor pressure of the water at working temperature. Thus, the cavitation is not considered [22]. The conservation equations for steady incompressible and isothermal flow, with zero gravitational and other external body forces,

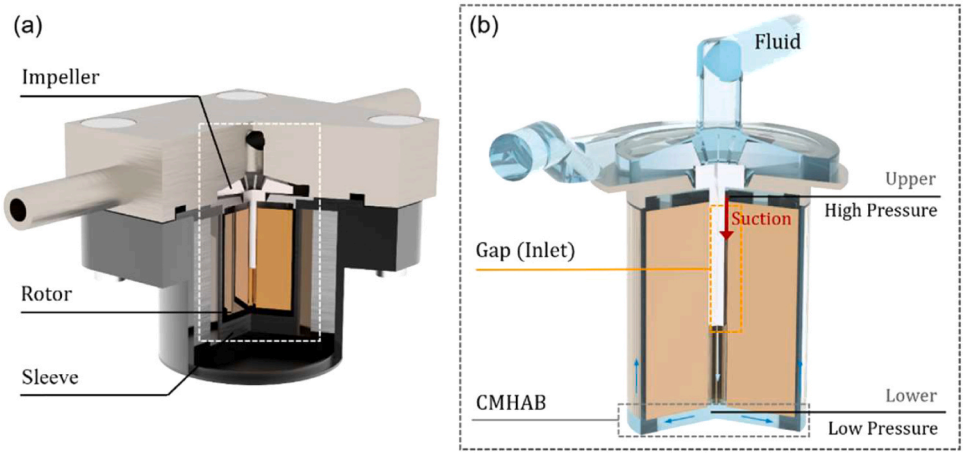

Fig. 1. (a) The structure of micropump with hydrodynamic bearing system (b) Fluidic channel in the micropump.

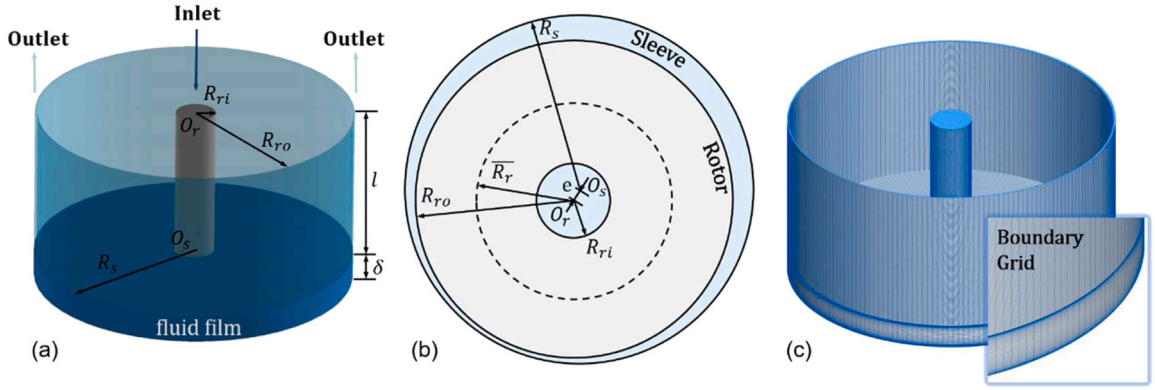

Fig. 2. (a) Three-dimensional computational fluid domain of CMHAB (b) Top view sketch of CMHAB (c) Computational mesh for the whole domain of CMHAB.

Table 1
CMHAB characteristics and operating conditions.

Parameter	Symbol	Value
CMHAB geometry parameters		
Inner/Outer diameter of rotor	D_{ri}/D_{ro}	1.6/12.66 mm
Inner diameter of sleeve	D_s	12.8 mm
Eccentric distance of rotor	e	0.035 mm
Computational domain height	l	(6 +δ)mm
Simulation operating conditions		
Flow rate	Q	15–35 ml/min
Rotational speed	n	15,000–25,000 rpm
Film thickness	δ	0.1–1.4 mm
Outlet pressure	P_m	30 kPa
Experiment operating conditions		
Flow rate	Q	180–280 ml/min
Rotational speed	n	8000–13000 rpm
Film thickness	δ	0.5–2 mm
Outlet pressure (rig)	P_r	101.3 kPa
Lubricant characteristics		
Type	–	Liquid-water
Temperature	T_f	25 °C
Density	ρ	998.2 kg/m^3
Viscosity	μ	0.001003 kg/(m•s)
Load capacity measurement rig parameters		
Inlet area/Outlet area	S_{in}/S_{out}	2.011/2.799 mm^2
Volume of liquid in the gap	$V_{interval}$	(124.69δ+56) mm^3

are:

Mass conservation equation:

$$\nabla \bullet V = 0 \tag{2}$$

Momentum equations:

$$\rho(V \bullet \nabla)V = -\nabla p + \nabla \bullet (\mu \nabla V) \tag{3}$$

2.1.4. Boundary conditions and fluid properties

The upper surface of the fluid domain of the rotor center hole is specified as the velocity inlet condition. Meanwhile, the upper surface of the clearance between the rotor and sleeve is defined as the outlet, the outlet condition differs according to working conditions. When simulating the working conditions of CMHAB in the sealed micropump, the outlet condition is set as the Pressure-outlet with pressure of 30*kPa*, yet it is set as Outflow while simulating the conditions of CMHAB in the rig. Considering that the rotor is rotating in the working state, the inner and outer sidewall, as well as the bottom surface of the rotor are set as rotational walls with the rotational speed of n. The surfaces of the sleeve, including the sidewall and the bottom surface, are specified as stationary walls. During the CFD simulations, the liquid-water is chosen as the only working medium in the fluid domain, which has a density of *998.2 kg/m^3* and a viscosity of *0.001003 kg/(m•s)* as its property parameters.

Table 2
The grid height of the first layer.

Position	Rotor			Sleeve	
	inner wall	outer wall	bottom surface	inner wall	bottom surface
grid height (μm)	6.9	1.5	1.5	5.6	4.3

Table 3
Grid independence study.

Mesh	Number of cells	Force
M1(tiny)	6,12,000	3.12244
M2(coarse)	10,15,175	3.1155
M3(medium)	16,64,000	3.11387
M4(fine)	36,35,000	3.1115
M5(extra-fine)	55,80,000	3.10891

2.1.5. Turbulence model and numerical method

The cost of direct numerical simulation of turbulent flow limits its application in the three-dimensional numerical simulation of the CMHAB. To determine the turbulence model for the numerical simulation, the results of five different turbulence models based on the URANS method are compared, the Realizable $k-\varepsilon$ model is finally found as the best-suited model for the present study, whose turbulent kinetic energy k and the turbulent kinetic energy dissipation rate ε equation [23] are as follows:

$$\frac{\partial}{\partial t}(\rho k)+\frac{\partial}{\partial x_i}(\rho k u_i)=\frac{\partial}{\partial x_j}\left[\left(\mu+\frac{\mu_i}{\sigma_k}\right)\frac{\partial k}{\partial x_j}\right]+G_k+G_b-\rho\epsilon-Y_M+S_k \tag{4}$$

$$\frac{\partial}{\partial t}(\rho k)+\frac{\partial}{\partial x_i}(\rho \epsilon u_i)=\frac{\partial}{\partial x_j}\left[\left(\mu+\frac{\mu_i}{\sigma_\epsilon}\right)\frac{\partial \epsilon}{\partial x_j}\right]+\rho C_1 F_\epsilon+C_{1\epsilon}\frac{\epsilon}{k}C_{3\epsilon}G_b-C_2\rho\frac{\epsilon^2}{\sqrt{k+\theta\epsilon}}+S_\epsilon \tag{5}$$

Where G_k represents the generation of turbulence kinetic energy due to the mean velocity gradients. The constants in the model $C_{1\epsilon}$, C_2, σ_k, σ_ϵ are 1.44, 1.9, 1.0, 1.2 respectively. And C_1 can be described by the following formula

$$C_1=\max\left[0.43,\frac{\eta}{\eta+5}\right] \tag{6}$$

And the modelling turbulent viscosity is represented as follows:

$$\mu_t=\rho C_\mu\frac{k^2}{\epsilon} \tag{7}$$

For spatial discretization of the momentum, turbulent kinetic energy, and turbulent dissipation rate, a second-order upwind scheme is employed. the pressure-velocity coupling is performed using the SIMPLE

algorithm. During the calculation, the convergence criterion for all residuals is set to 10^{-9}. Detailed numerical simulation results of the flow in the CMHAB operating at high speed are presented below.

2.1.6. Bearing performance evaluation index

This paper evaluates the performance of the CMHAB using three parameters [12,24]: load capacity W, friction torque T_f, friction force F_f, friction coefficient f. The load capacity, which is the total vertical force exerted on the rotor, is calculated by integrating the pressure over the rotor surface:

$$W = \int_0^{2\pi} \int_{\frac{D_2}{2}}^{\frac{D_1}{2}} p(r,\theta) r dr d\theta \tag{8}$$

The friction torque exerted to the rotor is calculated by integrating the torque of shear stress in the circumferential direction over the rotor surface:

$$T_f = \int_0^{2\pi} \int_{\frac{D_2}{2}}^{\frac{D_1}{2}} \tau_\theta r^2 dr d\theta \tag{9}$$

The friction force exerted to the rotor is calculated by integrating the shear stress over the rotor surface:

$$F_f = \int_0^{2\pi} \int_{\frac{D_2}{2}}^{\frac{D_1}{2}} \tau r dr d\theta \tag{10}$$

The friction coefficient f is the ratio of friction force to load capacity, which is defined as:

$$f = \frac{F_f}{W} \tag{11}$$

2.2. Experimental method

2.2.1. Measuring principle

The experimental rig is designed and constructed in this study to measure the load capacity exerting on the bottom of the rotor in the CMHAB at the situation that CMHAB is exposed to the atmosphere. The structure and components of the load capacity measurement rig are displayed in Fig. 3a-b, as the Fig. 3b shows a local enlarged section of the rig.

The rig is mainly composed of four parts: main structure, rotor driving part, liquid circuit and fluid film thickness adjustment part. The rotor drive part contains the power supply and motor, which can be used to adjust the rotor speed n. The liquid circuit includes a pump, related pipes and a valve used to regulate the flow rate Q. While the fluid film thickness adjustment part is composed of two XYZ axis displacement platforms and the thickness-limited pin, which aims to limit the thickness of the fluid film δ.

Fig. 3c shows the working principle of the CMHAB load capacity measuring rig. In this study, the load capacity of the CMHAB ($\vec{F}_{rotor}$) is difficult to measure directly for the rotor moving in the sleeve. Therefore, the following method is used to obtain the load capacity indirectly.

As the force imposing on the pressure sensor $\vec{F}_{measured}$ can be measured directly, the fluid film pressure exerting on the bottom of the sleeve $\vec{F}_{static}$ can be simply calculated by Eq. (12).

$$\vec{F}_{static} = \vec{F}_{measured} - \vec{G}_{sleeve} \tag{12}$$

In the formula, $\vec{G}_{sleeve}$ stands for the gravity of the sleeve.

From the force analysis of the fluid film at the bottom of the rotor, the fluid is only subject to the pressure of the rotor, the support force of the sleeve and its own gravity. According to the momentum theorem, the following equation can be derived.

$$\dot{m}(\vec{v}_{in} - \vec{v}_{out}) = \vec{F}_{static} + \vec{F}_{rotor} - \vec{G}_{water} \tag{13}$$

In the formula, $\vec{v}_{in}$ is the liquid inlet speed, $\vec{v}_{out}$ is the liquid outlet speed, $\dot{m}(\vec{v}_{in} - \vec{v}_{out})$ represents the momentum change of the fluid film formed between the bottom of the rotor and the sleeve. $\vec{G}_{water}$ is the gravity of the water between rotor sidewall and sleeve. Since $\dot{m}$, $\vec{v}_{in}$, $\vec{v}_{out}$, $\vec{F}_{static}$, $\vec{G}_{water}$ are all known quantities presently, the value of the CMHAB load capacity $\vec{F}_{rotor}$ can be finally determined.

2.2.2. Operation instruction

The instruction of load capacity measuring rig is as follows:

Before the official start of the measurement, rig initialization is required: Firstly, measure the weight of the sleeve and associated connecting parts when the rotor is not loaded using the pressure sensor located at the bottom of the sleeve and record the sensor indication as $F_0(|\vec{G}_{sleeve}| = F_0)$. Next, place the rotor inside the sleeve and install the thickness-limited pin.

And subsequent operations help to control the working parameters (δ, n, Q) of the rig: Adjust the Z direction knob of the XYZ axis displacement platform until the rotor sleeve contacts with the thickness-limited pin, resulting in a fluid film thickness of 0. Then, slowly twist the Z direction knob while observing the scale until the desired film thickness of δ is achieved. Therefore, the film thickness will achieve the desired value δ when the rotor is suspended due to the limiting effect. The rotor speed, n, can be adjusted by the power supply, and the flow

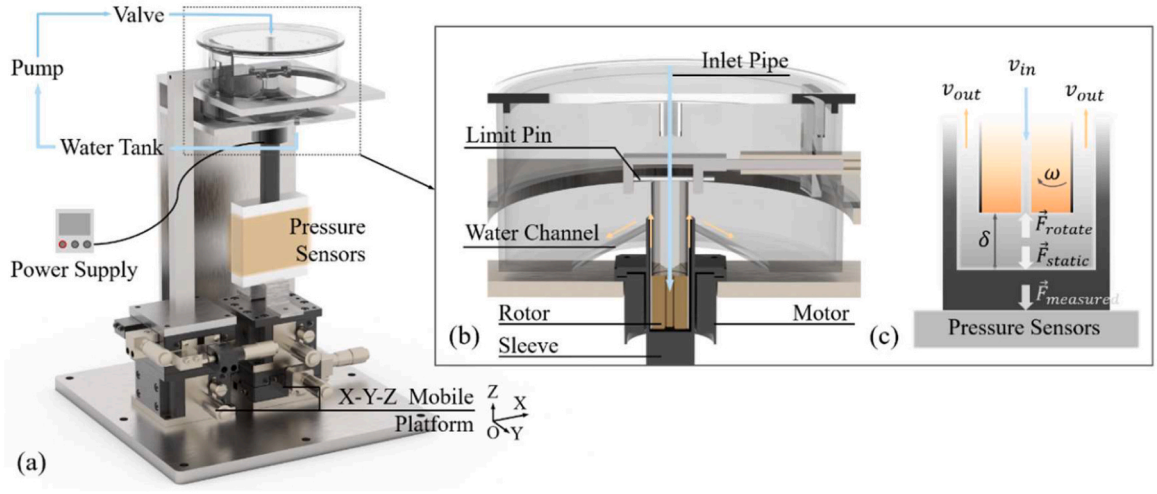

Fig. 3. (a) Load capacity measuring rig structure (b) Local enlarged section of the rig (c) Test principle schematic.

rate, Q, can be controlled by adjusting the valve opening. Once the rig starts operating steadily, record the pressure sensor indicator as $F_1(|\vec{F}_{measured}| = F_1)$. The load capacity on the rotor bottom can be calculated using the following formula.

$$\left|\vec{F}_{rotor}\right| = (F_1 - F_0) - \frac{\rho Q}{60} \bullet \left(\frac{Q}{60S_{in}} + \frac{Q}{60S_{out}}\right) - \rho V_{interval} g \tag{14}$$

In this formula, $(F_1 - F_0)$ is the difference between the two measured values, and the rest part is the value calculated by known experimental parameters. Among them, Q is the inlet-suction flow rate, ρ is the density of the working fluid and $V_{interval}$ represents the volume of liquid between rotor sidewall and sleeve.

3. Results and discussion

3.1. Modeling validation

The fluid in the micropump is hard to be observed and the load capacity is hard to be measured by the experiment because the micropump needs to possess favorable closure in the operating state. Therefore, the CFD simulation is used to calculate the fluid flow process of CMHAB in the micropump.

In order to verify the accuracy of the calculation, the present CFD mathematical model for hydrodynamic analysis in CMHAB is validated with the comparation between the experiment results and the results calculated by CFD model in the same conditions. The differences of load capacity between computational results and the experimental data are around 0.07–0.24 *N*. two results also have the same trend, that is, the load capacity increases with the flow rate at the same speed, which further proves the accuracy of the simulation. It is found that the deviation is within 10%. Fig. 4 presents the representative results of performance indices, illustrating an excellent agreement in the present CFD model.

3.2. Flow mechanism and parameters' influence in CMHAB

In CMHAB, the flow process and characteristics can elaborate the principle of load capacity, and some primary parameters can significantly impact the load capacity. In the actual operation of the CMHAB, the rotational speed and the inlet-suction flow rate stand out as the most crucial operating parameters, which directly affect the performance of CMHAB. Meanwhile, the fluid film thickness of the bearing can be regulated by adjusting the dimensions of specific components within the micropump. Thus, the fluid film thickness is investigated as an independent variable of interest.

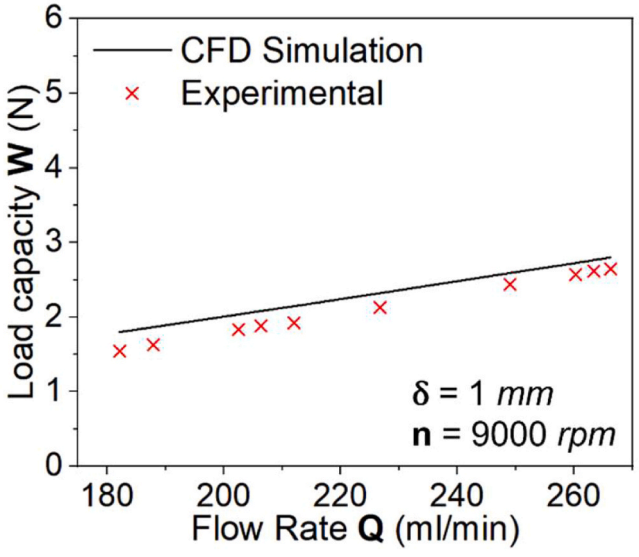

Fig. 4. Validation study. Comparison of proposed model-based results with the experimental results in the present work.

To conduct a comprehensive analysis of the CMHAB, we first analyze the flow process and characteristics, and examine the impacting laws and underlying mechanisms of these three variables: inlet-suction flow rate Q, rotational speed n, fluid film thickness δ.

3.2.1. The Analysis of the fluid flow mechanism in CMHAB

To simulate the flow of CMHAB, the bearing operating parameter (n, Q, δ) is set to (20,000 *rpm*, 25*ml/min*, 1 *mm*) based on the standard working condition of the micropump. The flow process and fluid characteristics in the CMHAB are depicted in Fig. 5. As the rotor rotates, the centrifugal action creates a low-pressure area at the center, drawing in fluid from the upper domain of the rotor center through the inlet. Upon entering the bottom basin of the rotor, the fluid rotates and flows radially due to the joint effect of viscous force and centrifugal force, forming a fluid film. Then, the fluid flows out through the outlet (Fig. 5a).

From the velocity distribution (Fig. 5b), there exists a region in the middle layer of the fluid film where the velocity distribution in the axial direction meets the following conditions. It is the core region of the fluid flow, where the fluid viscosity force is negligible and the fluid can be treated as a rigid body [25]. As a result, the radial speed of the fluid increases linearly with the radius (Fig. 5c).

$$\begin{cases} \dfrac{V_\theta}{\omega r} = C \\ V_r \to 0 \end{cases} \tag{15}$$

From the pressure distribution (Fig. 5d), fluid pressure increases along the radial direction due to centrifugation, while the axial pressure remains constant along the axial direction. In the low-pressure area, fluid is drawn fluid into the bearing since external pressure generates a pressure drop across this area. In the high-pressure area part, fluid generates a load capacity to suspend the rotor (Fig. 5c). These flow processes and characteristics provide the CMHAB with exceptional performance and stability.

3.2.2. Effect of the inlet-suction flow rate

To investigate the effect law of the inlet-suction flow rate in micropump, the load capacities under inlet-suction flow rate of 15–35 *ml/min* (known by numerical simulation results of micropump) are calculated for this flow rate range includes the whole working condition of micropump. As exhibited in Fig. 6a, the load capacity as well as its growth rate under each speed gradually increases as the inlet flow grows. Furthermore, under the condition of rotor speed $n = 20{,}000$ *rpm*, the load capacity increases 0.346 *N* as the inlet flow increases from 15 *ml/min* to 35 *ml/min*, which is 2.47 times of the rotor weight (0.14 *N*). In addition, the computed values of friction torque and friction coefficient at various inlet-suction flow rate are also presented. High inlet-suction flow rate brings stronger wall shear, leading to the corresponding increase in friction torque. But this effect is less pronounced compared with the load capacity, resulting in a decrease in friction coefficient.

Three control groups are set to explore the influences on the flow characters and the load capacity on the rotor at variable inlet flows, where takes $Q = 20$ *ml/min*, $Q = 25$ *ml/min* and $Q = 30$ *ml/min* at (n, δ) = (20,000 *rpm*, 1 *mm*) as numerical calculation conditions.

From the pressure distribution (Fig. 7), the trend that pressure varies with the rotor radius can be expressed by the following equation through numerical analysis. By comparison with the work of J. kurokawa [26] et al., an extra constant term K_i is found in the calculation formula of the pressure distribution. According to curve fitting, K_n almost remains unchanged under different Q, yet K_i is proportional to Q. Hence, K_i is considered to be brought by the inlet flow.

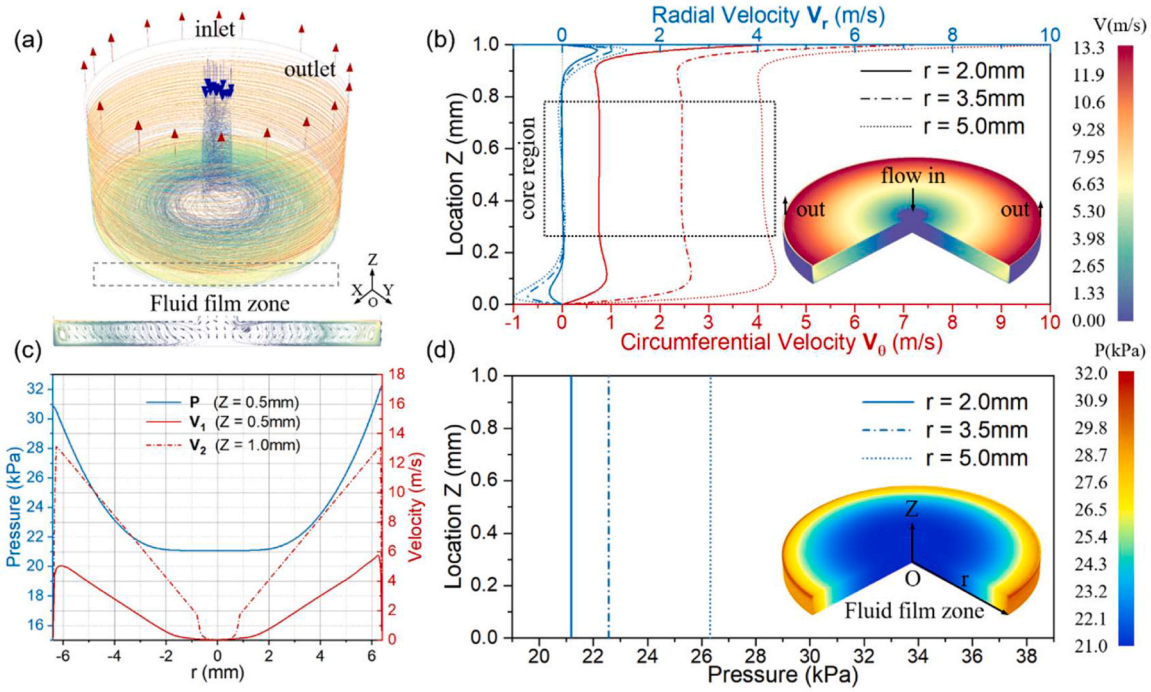

Fig. 5. (a) Streamline diagram in flow field of CMHAB (b) Velocity contour and velocity distribution on Z axis (axial direction) in CMHAB (c) Pressure/Velocity distribution in radial direction (d). Pressure contour and pressure distribution on Z axis in CMHAB.

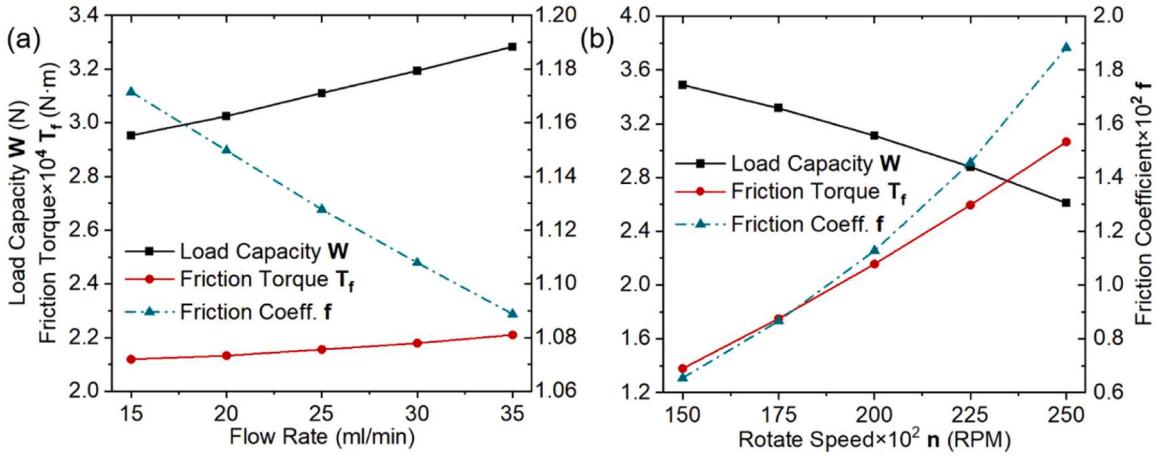

Fig. 6. (a, b) Computed values of load capacity, friction torque, and friction coefficient versus inlet suction flow rate and rotational speed, for CMHAB (The independent parameters are varied around the reference case values).

$$\frac{dP}{d(R_1 - r)} = K_n(R_1 - r) + K_i \tag{16}$$

However, the velocity distribution (Fig. 7b) reveals that the core region velocity varies a little with the inlet-suction flow rate, for the magnitude of inlet velocity is minute relative to the rotation speed.

The augmented fluid flow rate results in high turbulent disturbance and increased hydrodynamic pressure generation within the bearing fluid domain [27,28], thus enhancing the load capacity of CMHAB.

3.2.3. *Effect of the rotation speed*

To investigate the effect law of the rotational speed in micropump, the load capacities under 15,000–25,000 *rpm* are calculated for this speed range includes the whole working condition of micropump. As exhibited in Fig. 6b, the load capacity under each inlet-suction flow rate gradually decreases as the rotation speed grows, while its decline rate raising. Moreover, under the condition of inlet-suction flow rate Q = 25 *ml/min*, the load capacity reduces by 0.88 *N* as the rotation speed increases from 15,000 *rpm* to 25,000 *rpm*, which is 6.29 times as weight as the rotor. In terms of lubrication, the friction torque and rotational speed exhibit a linearly positive correlation, resulting in an increase in the friction coefficient as the rotational speed increases.

The conditions n = 17,500 *rpm*, n = 20,000 *rpm*, n = 22,500 *rpm* under $(Q, \delta) = (25\ ml/min, 1\ mm)$ are set in numerical calculation. In the circumstance of that outlet pressure is invariable, high rotational speed brings a heavy pressure gradience (Fig. 7c), thus, the pressure is lower at higher *n*. According to curve fitting, K_i almost remains unchanged under different *n*, yet K_n is proportional to n^2. Hence, K_n is considered to be brought by the speed.

Meanwhile, the velocity distribution in the core region follows the formula below, where K_{v1} is in proportion to *n* while K_{v2} depends on *Q*. (Fig. 7d)

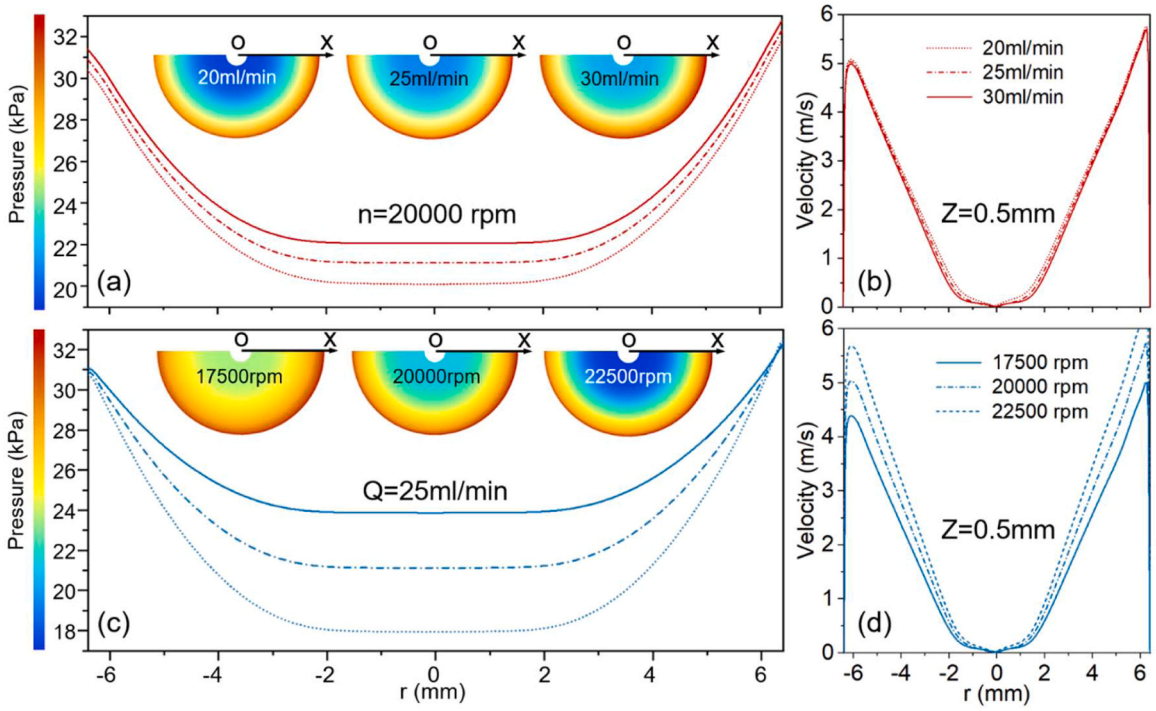

Fig. 7. (a, b) Computed values of pressure and velocity at (z = 0.5 *mm*, n = 20,000 *rpm*) versus the radial position under various inlet-suction flow rate, for CMHAB (c, d) Computed values of pressure and velocity at (z = 0.5 *mm*, Q = 25 *ml/min*) versus the radial position under various rotational speed, for CMHAB.

$$V(r) = K_{v1}r + K_{v2} \tag{17}$$

Therefore, a high rotational speed has greater contribution on the inlet-suction in CMHAB than the load capacity. It is worth mentioning that at higher rotating speeds, the increased pressure gradient causes an extra inlet flow, leading to a re-growth in load capacity. Oppositely, when the rotational speed is too low, the pressure gradient becomes tiny, and the suction effect at the inlet is weakened, which is not conducive to

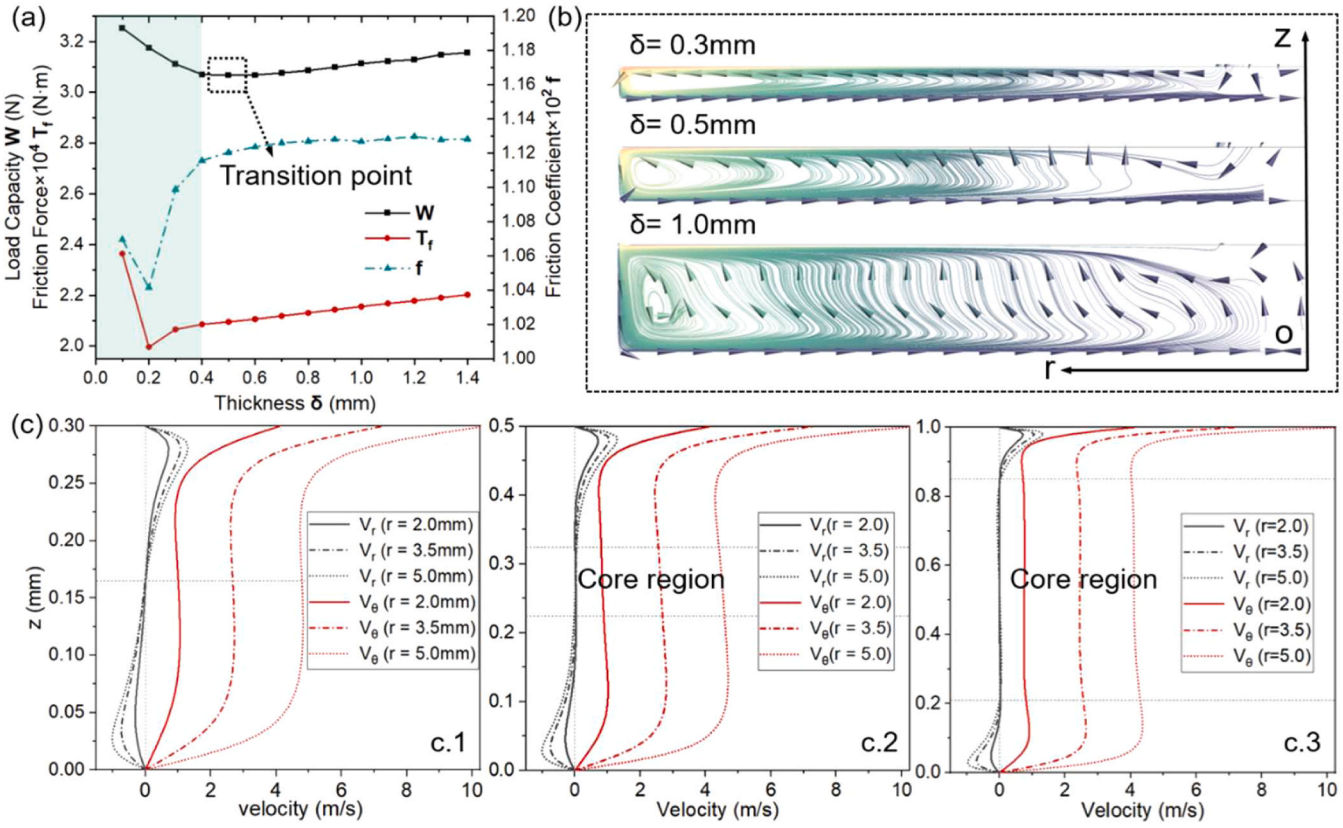

Fig. 8. (a) Computed values of load capacity, friction torque, and friction coefficient versus fluid film thickness, for CMHAB (b) Streamline diagram in flow field of CMHAB under various fluid film thickness (c) velocity distribution via Z at different radial position under various fluid film thickness.

the operation of the CMHAB. The specific numerical correspondence is in further exploration.

3.2.4. Effect of the fluid film thickness

To ensure the prevention of collision and blockage in our micropump, we have adopted a fluid film thickness of approximately 1 mm at the standard working condition in the current micropump design. This configuration has proven to be highly reliable through long-term operation and application of micropumps. Moreover, the micropumps have passed a series of reliable tests, which includes mechanical vibration test, impact test and high accelerated life test. However, present design mainly relies on experience and lacks theoretical guidance. The optimum fluid film thickness needs to be investigated and determined to improve bearing performance and micropump efficiency.

As exhibited in Fig. 8a, the load capacity decreases initially and then increases as the fluid film getting thicker. In the range of $\delta = 0.1$–0.5 *mm*, the load capacity decreases from 3.253 *N* to 3.067 *N*, representing a reduction of 1.33 rotor's weight, and reaches its minimum value at $\delta = 0.5$ *mm*. In the range of $\delta = 0.5$–1.4 *mm*, the load capacity increases from 3.067 *N* to 3.157 *N*, rising by 0.64 rotor's weight, but the slope of the curve is smaller than that of $\delta = 0.1$–0.5 *mm*. As the fluid film thickness grows, the friction torque decreases first and then increases, while the friction coefficient has the same trend. When $\delta = 0.5$–1.4 *mm*, the rising slope of the friction coefficient is gentle. The influence of film thickness on the friction properties is becoming weak due to the emergence of the core area.

Velocity curves at varying fluid film thicknesses are plotted to investigate the cause of the opposite changing trends within the range of $\delta = 0.1$–1.4 *mm*. At thin fluid film thicknesses ($\delta = 0.1$–0.5 *mm*), interference occurs between two boundary layers and the core region is nonexistent (Fig. 8c). As the fluid film getting thicker, the energy dissipation due to secondary flow patterns within the fluid film increases, resulting in a significant decrease in the load capacity. However, at around 0.5 *mm*, two boundary layers separate and core region emerges [29,30]. In consequence, it is speculated that the reversed trend is derived from the appearance of the core region.

As the gradient $-dW/d\delta$ is an indicator of bearing stiffness (the steeper the curve, the stiffer the bearing), the CMHAB possesses proper stiffness when $\delta = 0.1$–0.3 *mm*. Considering stiffness, anti-abrasion property and lubrication, the stability of the CMHAB can be effectively improved by controlling the fluid film thickness at the bottom of the rotor to be around 0.3 *mm* at the standard working condition. In comparison to the current micropump design, the proposed approach would result in the reduction of the axial dimension of the sleeve. As a consequence, the fluid flow entering the bearing area would be constrained, leading to an enhancement in the hydraulic efficiency of the micropump.

3.3. Actual operation and performance of CMHAB

Fig. 9a shows the physical diagram of the CMHAB load capacity measuring rig. In the experiment, the rotor rotates smoothly in the sleeve, and the suspension of the rotor is grossly stable. This phenomenon is clearly observed in Fig. 9: the position of the rotor when the rig is not started is shown in Fig. 9b-off, where the bottom of the rotor is in contact with the bottom of the sleeve, and the upper end of the rotor sleeve is at a distance from the thickness-limited pin. Fig. 9b-on shows that when the rig is in motion, where the rotor is suspended by hydrodynamic power, and the rotor bottom leaves the bottom of the sleeve while the upper surface of the rotor top is in contact with the thickness-limited pin. This experimental phenomenon proves that the fluid film has a bearing capacity effect on the rotor, and the rotor can realize axial suspension. Besides, CMHAB possesses high performance and prominent stability in micropumps, as hydraulic performance of micropumps with

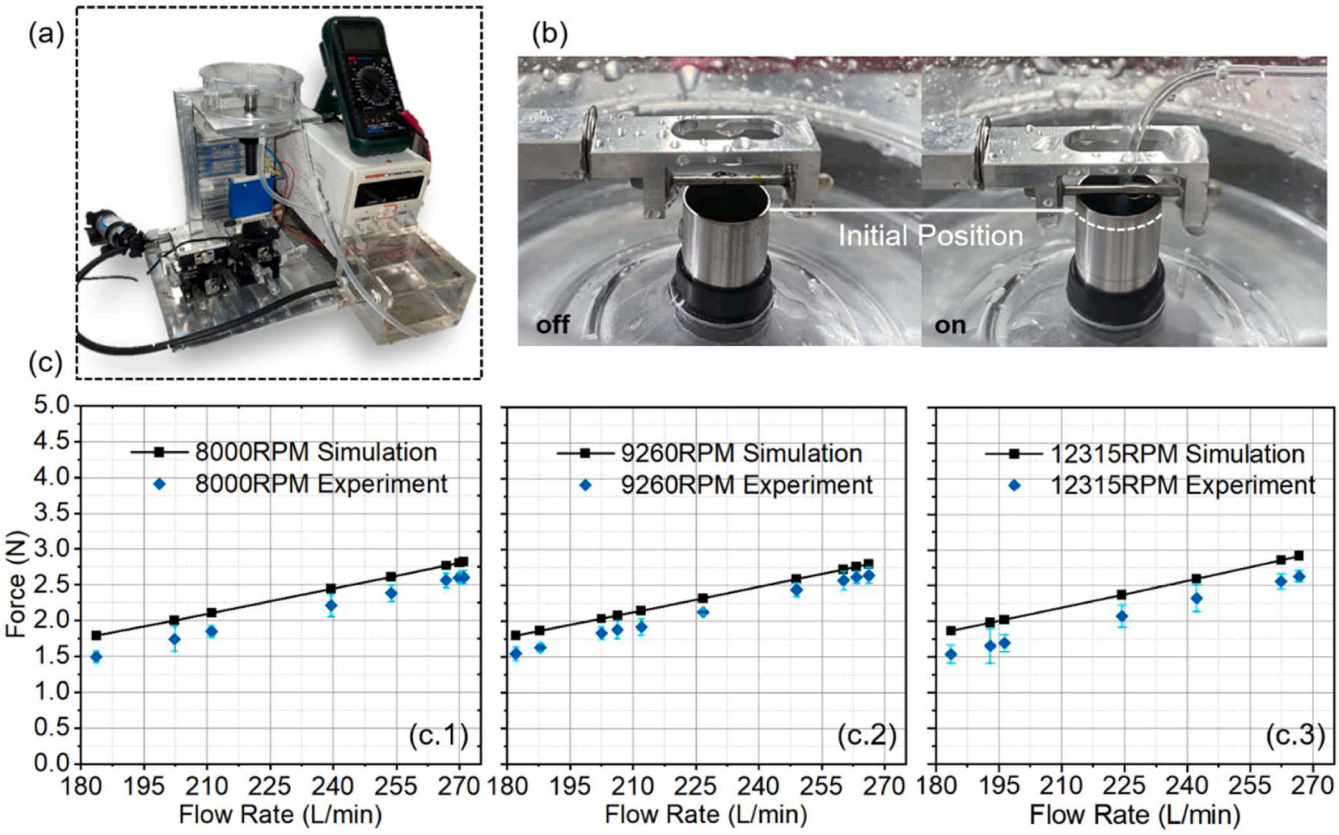

Fig. 9. (a) Photograph of developed load capacity measuring system (b) Rotor positions at different condition (rig on/rig off) (c) The measurement value under various conditions and the comparison of numerical analysis and experimental values.

the CMHAB is examined to be outstanding in our previous study [6].

While the thickness of the fluid film is maintained at $\delta = 1$ *mm*, the load capacity is measured at different flow rates for various rotational speed of $n = 8000$ *rpm*, 9260 *rpm*, 12,315 *rpm*. To avoid fortuitous results in the experiment, repeated measurement is applied with the CMHAB load capacity measured three times under the same condition, and standard deviations of three measured values are calculated. The change curve of the load capacity with flow rate is obtained, and the values of load capacity on the bottom of the rotor with flow rates at different speeds are shown in Fig. 9c. The abscissa represents the flow rate, and the ordinate represents the load capacity on the bottom of the rotor. As can be seen from the figure, the load capacity increases as the flow rate grows. All standard deviations are within 0.35 *N* and no more than 18% of simulated values and 22% of measured values.

4. Conclusion

The current investigation clarifies the inherent mechanism of the novel centrifugal micro hydrodynamic axial thrust bearing (CMHAB) and reports its performance under various operating parameters. To assess the load capacity of the bearing in the sealed environment, CFD simulation is utilized due to monitoring difficulties. Moreover, experiments are conducted to examine its performance and systematically vary parameters in the actual condition. The investigations outlined in this paper lead to the following conclusions:

1. The CMHAB's mechanism involves a combination of centrifugation and inlet-suction. Due to the high rotational speed of the rotor in the CMHAB, a low-pressure zone is formed that allows fluid to be drawn into the bearing domain. Meanwhile, the pressurized fluid generates load capacity on the rotor.
2. Load capacity exhibits an increase with the inlet-suction flow rate *Q*, a decrease with the rotational speed. When the fluid film thickness varies from 0.1 *mm* to 1.4 *mm*, the load capacity initially decreases and then increases, with $\delta = 0.5$ *mm* representing the critical point.
3. To further optimize the CMHAB, $\delta = 0.3$ *mm* should be selected as it represents the fluid film thickness with the proper bearing stiffness and favorable anti-abrasion property for micropumps. Based on this finding, the structural size of the micropump will be adjusted to enhance its operational stability and hydrodynamic efficiency.
4. A load capacity measurement rig of micro hydrodynamic axial-thrust bearing is proposed in this paper. The measuring results obtained from the experiments agree well with the theoretical analysis, providing confidence in the accuracy of our theories.

The findings provide a more comprehensive understanding of the physical mechanisms involved in CMHAB. This understanding holds potential for CMHAB's application to other fields.

Declaration of Competing Interest

The authors declare that they have no known competing financial interests or personal relationships that could have appeared to influence the work reported in this paper.

Data availability

Data will be made available on request.

Acknowledgements

The authors would like to acknowledge the financial support by National Key R & D Project from Ministry of Science and Technology of China (Grant No. 2022YFA1203100) and National Key Research and Development Program of China (2022YFC2204400).

References

[1] Kim J, Kim S, Choi J, Koo C. A 3D Miniaturized glass magnetic-active centrifugal micropump fabricated by SLE process and laser welding. Micromachines 2022;13 (8):1331.
[2] Nguyen N, Huang X, Chuan TK. MEMS-micropumps: a review. ASME. J. Fluids Eng, 124; 2002. p. 384–92.
[3] Watterson PA, Woodard JC, Ramsden VS, Reizes JA. VentrAssist hydrodynamically suspended, open, centrifugal blood pump. Artif Organs 2000;24(6):475–7.
[4] Wu R., Duan B., Liu F., Wu H., Cheng Y., Luo X. Design of a hydro-dynamically levitated centrifugal micro-pump for the active liquid cooling system, 18th International Conference on Electronic Packaging Technology (ICEPT) 2017; 402–406.
[5] Luo X.B., Liu F.L., Duan B., Wu H., Hu J.Y., Yu X.J. A hydrodynamic levitated mechanical micropump, US Patent, 2016, US 10495093.
[6] Xing G, Xue S, Hong T, Zuo H, Luo X. A novel hydrodynamic suspension micropump using centrifugal pressurization and the wedge effect. Sci China Technol Sc 2023. https://doi.org/10.1007/s11431-022-2306-9.
[7] Osterle F, Charnes A, Saibel E. On the solution of the reynolds equation for slider-bearing lubrication—IX: The stepped slider with adiabatic lubricant flow. Asme Trans 1955;77(8):1185–7.
[8] Naduvinamani NB, Fathima ST, Hiremath PS. Hydrodynamic lubrication of rough slider bearings with couple stress fluids. Tribol Int 2003;36:949–59.
[9] Lai T, Guo Y, Wang W, Chen S, Hou Y. Experimental study on multi-decked protuberant foil thrust bearing with different number of thrust pads. J Adv Mech Des Syst Manuf 2016;10(9).
[10] Atwal JC, Pandey RK. Film thickness and friction investigations in a fluid film thrust bearing employing a new conceived micro-texture on pads. Asme J Tribol 2021;143(6):061801.
[11] Hamilton DB, Walowit JA, Allen CM. A theory of lubrication by micro-irregularities. Asme J Basic Eng 1966;88(1):177–85.
[12] Papadopoulos CI, Kaiktsis L, Fillon M. Computational fluid dynamics thermohydrodynamic analysis of three-dimensional sector-pad thrust bearings with rectangular dimples. Asme J Tribol 2014;136(1):011702.
[13] Aggarwal S, Pandey RK. Frictional and load-carrying behaviours of micro-textured sector shape pad thrust bearing incorporating the cavitation and thermal effects. Lubr Sci 2017;29(4):255–77.
[14] Siripuram RB, Stephens LS. Effect of deterministic asperity geometry on hydrodynamic lubrication. Asme J Tribol 2004;126(3):527–34.
[15] Aggarwal S, Pandey RK. Performance investigation of micro-pocketed textured pad thrust bearing. Ind Lubr Tribology Ind Lubr Tribo 2018;70:1388–95.
[16] Yu H, Wang X, Zhou F. Geometric shape effects of surface texture on the generation of hydrodynamic pressure between conformal contacting surfaces. Tribol Lett 2010;37:123–30.
[17] Wang H, Lin N, Yuan S, Liu Z, Yu Y, Zeng Q, Li D, Fan J, Wu Y. Numerical simulation on hydrodynamic lubrication performance of bionic multi-scale composite textures inspired by surface patterns of subcrenata and clam shells. Tribol Int 2023;181:108335.
[18] Atwal JC, Pandey RK. Performance analysis of thrust pad bearing using micro-rectangular pocket and bionic texture. Proc I Mech E Part J: J Eng Tribol 2021;235 (6):1232–50.
[19] Shen C, Khonsari MM. Numerical optimization of texture shape for parallel surfaces under unidirectional and bidirectional sliding. Tribol Int 2015;82:1–11.
[20] Fesanghary M, Khonsari MM. Topological and shape optimization of thrust bearings for enhanced load-carrying capacity. Tribol Int 2012;53:12–21.
[21] Zhu B, Zhang W, Zhang W, Li H. Generative design of texture for sliding surface based on machine learning. Tribol Int 2023;179:108139.
[22] Xue S, Xing G, Hong T, Zuo H, Luo X. Numerical investigation of cavitation flow characteristics in a hydrodynamic levitated micropump with eccentric rotation. Int J Appl Mech 2023;15(2):2350010.
[23] Shih TH, Liou WW, Shabbir A, Yang ZG, Zhu J. A new k-ε eddy viscosity model for high reynolds number turbulent flows. Comput Fluids 1995;24(3):227–38.
[24] Papadopoulos CI, Efstathiou EE, Nikolakopoulos PG, Kaiktsis L. Geometry Optimization of Textured Three-Dimensional Micro- Thrust Bearings. Asme J Tribol 2011;133(4):041702.
[25] Batchelor GK. Note on a class of solutions of the navier-stokes equations representing steady rotationally-symmetric flow. Q J Mech Appl Math 1951;4(1): 29–41.
[26] Kurokawa J, Toyokura T. Study on the axial thrust of the radial flow turbomachinery, 2th International JSME Symposium Fluid. Machinery and Fluidics 1972.
[27] Olver AV, Fowell MT, Spikes HA, Pegg IG. 'Inlet suction', a load support mechanism in non-convergent, pocketed, hydrodynamic bearings. Proc I Mech E Part J: J Eng Tribol 2006;220(2):105–8.
[28] Fowell MT, Olver AV, Gosman AD, Spikes HA, Pegg IG. Entrainment and inlet suction: two mechanisms of hydrodynamic lubrication in textured bearings. Asme J Tribol 2007;129(2):336–47.
[29] Daily JW, Nece RE. Chamber dimension effects on induced flow and frictional resistance of enclosed rotating disks. Asme J Basic Eng 1960;82(1):217–30.
[30] Schröder TR, Dohmen HJ, Brillert D, Benra FK. Impact of leakage inlet swirl angle in a rotor–stator cavity on flow pattern, radial pressure distribution and frictional torque in a wide circumferential reynolds number range. Int J Turbomach Propuls Power 2020;5(2):7.